

Copyright 1995 Society of Photo-Optical Instrumentation Engineers. This paper was published in {*X-Ray and Extreme Ultraviolet Optics*}, Richard B. Hoover and Arthur B. Walker, Eds., Proceedings of SPIE Vol. Vol. 2515, p. 391, and is made available as an electronic reprint with permission of SPIE. One print or electronic copy may be made for personal use only. Systematic or multiple reproduction, distribution to multiple locations via electronic or other means, duplication of any material in this paper for a fee or for commercial purposes, or modification of the content of the paper are prohibited.

AXAF VETA-I Mirror X-ray Test Results Cross Check with the HDOS Metrology Data

Ping Zhao and Leon P. Van Speybroeck

Harvard-Smithsonian Center for Astrophysics
60 Garden Street, Cambridge, MA 02138

ABSTRACT

The AXAF VETA-I mirror X-ray test results have been cross checked with predictions based upon the HDOS metrology measurements and calculations of the effects of imperfect test system geometry and mirror mount induced distortions. The cross check was done by comparing the VETA-I X-ray test results with a VETA-I model, which is a computer simulation of the VETA-I mirror performance during the X-ray test. The HDOS (Hughes Danbury Optical Systems, Inc., Danbury, CT) metrology measurements (with CIDS, PMS, and WYKO) were performed after the VETA-I X-ray test in order to determine the surface figure errors of the mirror pair, including the overall surface map and the surface roughness. Mirror performance was predicted based on the measured surface figure errors and X-ray scattering theory.

All the VETA-I X-ray test data (FWHM, encircled energy, effective area, wing scan, and ring focus) were cross checked with the HDOS metrology measurements. The results of this study show reasonably good agreement between the X-ray test data and the metrology data. Similar analysis should be performed for the HRMA mirrors, which is an important step in securing a scientifically successful AXAF mission.

Keywords: AXAF, VETA-I, X-ray mirror, surface roughness, scattering, ray-trace

1 VETA-I X-RAY TEST

The Verification Engineering Test Article I (VETA-I) was the uncoated and uncut outermost pair of the HRMA – the heart of the AXAF-I. The two VETA-I mirrors are called P1 (paraboloid) and H1 (hyperboloid). A test of the mirror surface quality was successfully performed at the X-ray Calibration Facility (XRCF) of the Marshall Space Flight Center from September 1 to October 18, 1991.

X-rays generated by an electron impact source [1] 528 meters away were focused by the VETA-I to its focal plane, which is 10 meters behind the VETA-I. The focused X-rays were then detected and measured with the VETA X-ray Detecting System (VXDS) which consists of two types of detectors – the gas Proportional Counter (PC) and the High Resolution Imager (HRI). Because the P1 and H1 were not cut to the design length, they had to be spaced 109.03 mm farther apart than the design spacing during the test (this fact is called “despace”). The mirror is designed to focus incident X-rays from infinitely distant sources. For the ground test with a finite source distance and despace, there are two interesting focal planes where our measurements were made [2]. One is called the overall focal plane or the finite-distance focal plane (hereafter referred to as the focal plane), and is located farther away from the mirror than the designed focal length. This is the location of the waist of X-rays focused by the entire mirror. The other is called the ring-focus plane and is located in between the on-orbit focal plane and the finite-distance focal plane. In the ring-focus plane, X-rays form a sharply focused ring before reaching the focal plane. The ring focus is caused by spherical aberration due to the finite source distance and the despace in the VETA-I test [2, 3].

Five types of measurements were made during the VETA-I test:

- In the focal plane:
 - Full Width Half Maximum (this was the main goal of the VETA-I test).
 - Encircled energy.
 - Effective area.
 - Wing scan.

- In the ring focus plane:
 - Ring focus.

The results of these measurements were discussed in 18 papers published in the SPIE '92 and '93 proceedings [4].

2 HDOS METROLOGY DATA

After the X-ray test, VETA-I mirrors were shipped back to Hughes Danbury Optical Systems, Inc. (HDOS) in Danbury, CT. The mirror surface metrology measurements were performed in the fall of 1993. The instruments used were the CIDS (circularity and inner diameter station), the PMS (precision metrology station), and the MPMI or WYKO (Micro Phase Measuring Interferometer, a slightly modified WYKO Corporation instrument). The CIDS was used to determine circularity and the inner diameters. The PMS was used to measure along a meridian. With these two instruments, HDOS essentially measured both the ‘hoops’ and ‘staves’ of each barrel, and thus mapped the entire surface. Finally, microroughness was sampled on the VETA-I mirror P1 using the WYKO.

The primary data used for this analysis were HDOS map files for low frequency errors and HDOS WYKO files for higher frequency errors.

The map files represent a combination of PMS axial scan data and CIDS circularity data. The actual files used were p1p71_288.smp;1 and h1p74_288_map.smp;1. Each of these files had solid body translations and rotations removed and was then divided into two complementary maps by passing the data through a filter; the low pass portions were combined with the calculated mount induced distortions (see Section 3.3), fit with spline functions, and used deterministically in the ray-tracing. The high frequency portions were combined with the WYKO data and treated statistically. The standard HDOS filter was used for the separation; the parameters were such that the transition between low and high frequency passbands occurred from 0.02 to 0.03 mm^{-1} .

The WYKO data were taken as part of the evaluation of the “WYKO on a Stick” concept, and exist only for P1; consequently the same WYKO data had to be used for H1. The data for each WYKO magnification were combined into mean PSD files, and these files were used with the program “foldw1” (which is similar to the HDOS program eegraz) to calculate scattering distributions. The calculation was based on the scattering theory by Beckmann and Spizzichino [5]. These scattering distributions were used by a post-processing program to calculate image distributions. The PSD files do not agree perfectly in the overlap regions, so a linear weighting was used in the overlap regions such that the weight given to the lower frequency file would decrease from 1.0 to 0.0 while the weight given to the high frequency file would increase from 0.0 to 1.0. The frequency intervals are given in Table 1.

Table 1. Frequency intervals for psd files

Description	Frequency Interval (mm^{-1})		Data Source
	low	high	
P1 Low Frequency	0.001	0.4	p1p71_288.smp;1
P1 x2.5	0.4	4.0	WYKO x2.5 data
P1 transition x2.5-x20.0	4.0	12.0	WYKO x2.5 and WYKO x20.0 data
P1 x20.0	12.0	1000.0	WYKO x20.0 data
H1 Low Frequency	0.001	0.4	h1p74_288_map.smp;1
H1 x2.5	0.4	4.0	WYKO x2.5 data
H1 transition x2.5-x20.0	4.0	12.0	WYKO x2.5 and WYKO x20.0 data
H1 x20.0	12.0	1000.0	WYKO x20.0 data

The VETA-I surface PSD derived from the HDOS metrology data were plotted in Figure 1 as a function of the surface spatial frequency f . The solid line called “Combined PSD” is derived by linear weighting as mentioned above, which is used for the cross check with the X-ray test data. Surface roughness RMSs in three different frequency bands were calculated by substituting the Combined PSD into equation (6) (see Section 3.7). The results are shown on the upper right corner of the figure. Also plotted in Figure 1 is the PSD derived from the VETA-I wing scan

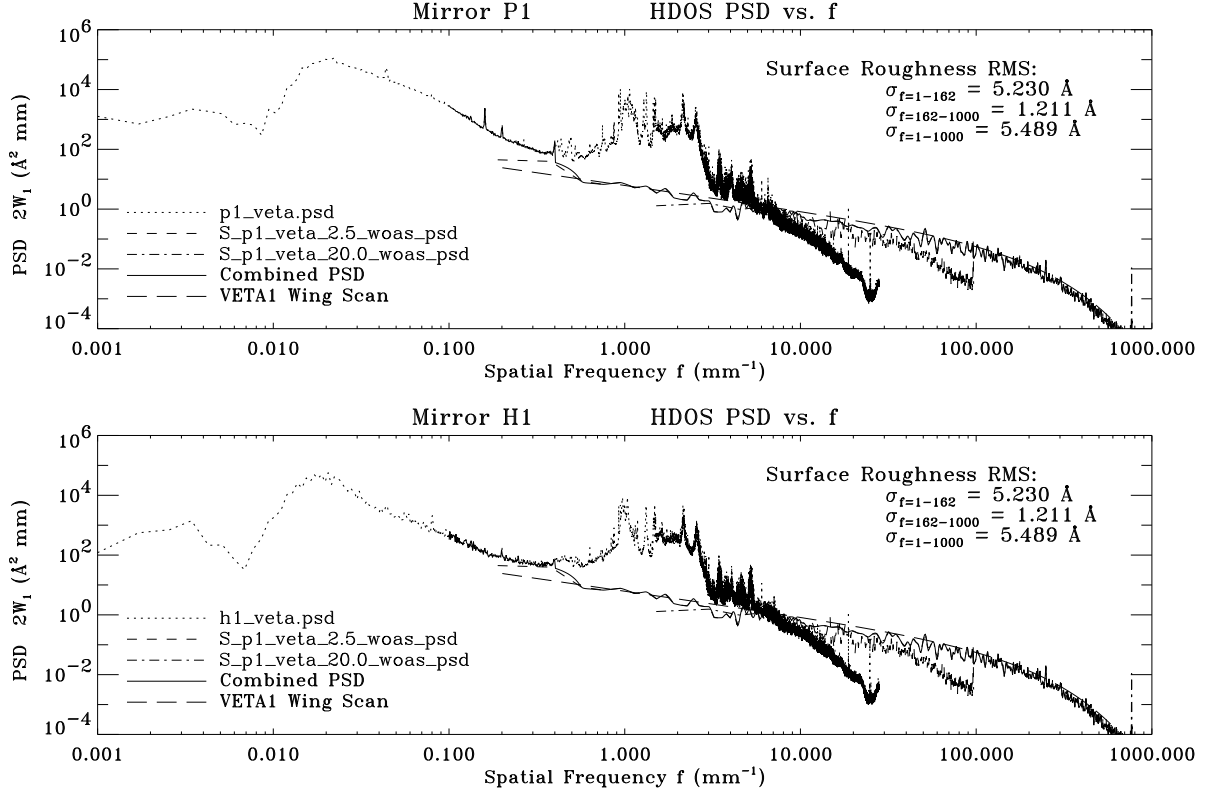


Figure 1: Surface PSDs of P1 and H1 derived from the HDOS metrology measurements, compared with the PSD derived from the VETA-I wing scan measurements.

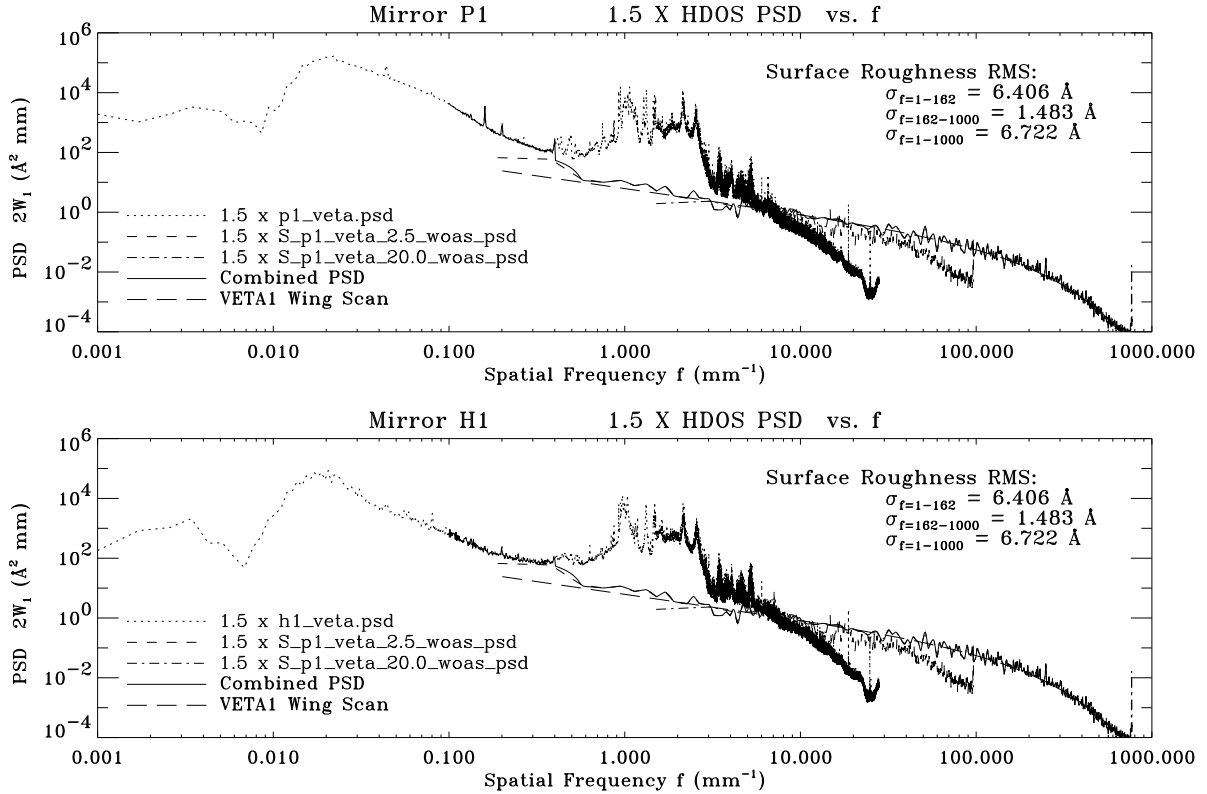


Figure 2: HDOS PSDs $\times 1.5$, compared with the PSD derived from the VETA-I wing scan measurements. The wing scan PSD is only sensitive in the frequency band of $f = 1 - 162 \text{ mm}^{-1}$.

data (see Section 3.7). It is seen that the wing scan PSD is slightly higher than the HDOS Combined PSD. Figure 2 shows the same plots with the HDOS surface PSD increased by a factor of 1.5, which agrees well with the wing scan data.

3 VETA-I MODEL

The VETA-I model is a computer simulation of the performance of the VETA-I mirrors during the X-ray test. It was built according to our best knowledge of the VETA-I test system and the mirror surface figure errors from the HDOS metrology data. The expected VETA-I X-ray test data were generated by ray-tracing which simulates the X-rays passing through the VETA-I model. Physical processes such as reflection, surface scattering, dust scattering, detector response, etc., were all simulated with the ray-trace.

The following is a list of elements built into the VETA-I model. The HDOS metrology data are implemented in mirror surface errors and mirror surface roughness scattering.

1. VETA-I mirror geometry
 - (a) Uncut mirror length
 - (b) P1 – H1 despace
 - (c) Supporting struts
 - (d) Apodizers
2. Test system geometry:
 - (a) Finite source size
 - (b) Finite source distance
3. Mount induced distortions:
 - (a) Gravity & compensation
 - (b) Thermal effects
 - (c) Epoxy shrinkage distortions
 - (d) Alignment fixture release distortions
4. Mirror surface reflection
5. Mirror surface errors
6. Mirror surface roughness scattering
7. Mirror surface dust scattering
8. HRI detector resolution

3.1 VETA-I Mirror Geometry

VETA-I mirrors are Wolter Type I grazing incidence mirrors consisting of a P1 (paraboloid) and a H1 (hyperboloid), made of Zerodur. The entrance of P1 has a diameter of ~ 1.23 m. Both P1 and H1 have the same design length – 838.2 mm.

Uncut mirror length: The VETA-I test was made with the mirror pair that was not cut to the design length. Their actual lengths were 990.51 mm and 990.73 mm for P1 and H1, respectively.

P1 – H1 Despace: Because the P1 and H1 were not cut to the design length, they had to be spaced 109.03 mm farther apart than the design spacing during the test. This is called “despace”.

Supporting Struts: Supporting struts were placed in between P1 and H1 during the test. They were 76.2 mm wide and oriented at $\pm 45^\circ$ and $\pm 135^\circ$.

Apodizers: Apodizers were used to block unwanted X-rays (due to uncut length and despace) from reaching the detector. They were placed at the back end of both mirrors and, as measured radially inward from the optical surface, 1.22 mm for P1 and 1.09 mm for H1 (see Section 4.2 for more details).

3.2 Test System Geometry

Finite source distance: The X-ray source for the VETA-I test was 528.74 meters from the front end of the P1.

Finite source size: The actual size and the intensity distribution of the X-ray source were measured before the VETA-I test with a pinhole camera [1]. The source model was built according to that measurement.

3.3 Mount Induced Distortions

Models of Mount Induced Distortions to the VETA-I mirror were produced by SAO, based on the best of our knowledge of the VETA-I test system.

Gravity & compensation: At the beginning of the VETA-I test, it was found from measurements in the focal plane that the mirror was ovalized under the earth's gravitation, i.e. the mirror diameter in the horizontal direction is slightly larger than that in the vertical direction. This distortion was promptly corrected by applying squeezing forces on the two sides of the mirror. This was called the gravity compensation for the global effect. But the gravity also had local effects due to the 12 flexure mounts, which were not compensated. Since the mirrors were hung from 12 invar pads (2 inch \times 2 inch) attached to the flexures, the gravity caused local distortions at those 12 locations. The distortions along the sides of the mirror were more severe than at the top or bottom. These local distortions would cause a shifted 12-fold symmetry (i.e. near 11 or 13 fold) and possibly a 2-fold symmetry due to the fact that the side distortions were different from the top and bottom. An over or under squeezed mirror would also have a 2-fold symmetry. All these multi-fold symmetries can be revealed by the ring focus measurements.

Thermal effects: The 12 flexures were attached to an aluminum ring which has a high thermal expansion coefficient. In contrast, the Zerodur mirror is well known for its extremely low thermal expansion. If the test temperature was different from the temperature when the mirror was mounted, the aluminum ring would pull or push the mirror through the flexures and the invar pads at those 12 mounting locations. A uniform thermal effect should cause a symmetric distortion on the mirror and therefore a 12-fold symmetry in the ring focus image. A non-uniform thermal effect could cause an asymmetric distortion on the mirror.

Epoxy shrinkage distortions: The shrinkage of epoxy between the invar pads and the mirror could cause local distortions in the mirror plane as well as in the direction normal to this plane. Assuming the amount of the epoxy is about the same under each pad, this distortion is also symmetric and hence produces a 12-fold symmetry in the ring focus image.

Alignment fixture release distortions: Each cylinder of VETA-I mirrors was supported upright when it was bonded to the 12 flexures. Then this support was released, and the mirror was placed sideways for the test. The caused distortions are called alignment fixture release distortions.

3.4 Mirror Surface Reflections

The mirror surface reflections were calculated based on the optical constant tabulated by Henke [6]. The mirror surface material is assumed to be pure Zerodur.

3.5 Mirror Surface Errors

The mirror surface errors, i.e. the actual surface deviations from the designed surface, were represented by surface maps of P1 and H1, derived from the low pass portions of the HDOS map data (see Section 2). The actual mirror surface in the VETA-I model is a spline fitted surface of the combination of the mount induced distortions and the HDOS surface maps.

3.6 Mirror Surface Roughness Scattering

The mirror surface roughness was represented by the surface PSD derived from the high frequency portion of the HDOS map data and the HDOS WYKO data (see Section 2). Since the WYKO data were only available for P1, the surface PSD of $f > 0.4 \text{ mm}^{-1}$ for both P1 and H1 were derived from the same WYKO data. These PSD files were used with the program "foldw1", a fortran routine as part of the **mirror** program, to calculate the scattering distributions on surface reflection. The calculation was based on the scattering theory by Beckmann and Spizzichino [5].

3.7 Mirror Surface Dust Scattering

The mirror surface dust scattering was simulated empirically in the focal plane according to the VETA-I wing scan data. The model used was mainly based on studies by Steve O'Dell [7] and Ron Elsner [8].

It is evident that the VETA-I mirror surface was contaminated with small particles (dust). During the VETA-I ring focus measurements, four quadrant ring images were taken with HRI at 215.3 mm from the focal plane, with a C-K source; one full ring image was taken with HRI at 159.2 mm from the focal plane, with an Al-K source (see ref. [2] for the images). Using these images, we can quantitatively display the effect of surface dust scattering. Figure 3 shows the relative intensity of scattered photons around the ring, based on the four quadrant ring images. The top panel shows the intensity of photons scattered inside the ring as a function of the azimuthal angle. Zero degree is at the bottom of the ring. The bottom panel shows the intensity of photons scattered outside the ring. Figure 4 shows the relative intensity of photons scattered inside the ring for full ring image. (The intensity of photons scattered outside the ring is not plotted for this image since the ring is too close to the edge of the HRI). It is seen that: 1) There are more scattered photons at the bottom of the ring; 2) The intensity difference between the bottom and the top of the ring is larger for the C-K source (Figure 3, factor of ~ 4) than that for the Al-K source (Figure 4, factor of ~ 2). This indicates that: 1) there is more dust at the bottom of the VETA-I mirror surface than that at the top; 2) the effect of dust scattering is more dominant at lower energies (i.e. C-K) than at higher energies (i.e. Al-K).

O'Dell and Elsner developed a simple model for the dust scattering. In fitting the VETA-I wing scan data, they assume the total scattering is a combination of the surface roughness scattering and the dust scattering. The scattering by dust goes approximately as θ^{-2} (θ is the scattering angle); while scattering by surface roughness goes approximately as $\lambda^{-2}\theta^{-2}$. Thus, scattering by dust dominates at long wavelengths; scattering by surface roughness dominates at short wavelengths.

To produce the dust scattering table for the VETA-I model, we slightly modified the formula used by O'Dell and Elsner. The power spectral density (PSD), $2W_1$, of the VETA-I surface is a function of spatial frequency, f , and the X-ray wavelength, λ . f and $2W_1$ (given in units of mm^{-1} and $\text{\AA}^2\text{mm}$, respectively) are defined as follows [9]:

$$f = \frac{\theta \sin \alpha}{\lambda} \quad (1)$$

$$2W_1(f, \lambda) = \frac{f\psi(\theta)\lambda^4}{8\pi \sin^4 \alpha} \quad (2)$$

where

θ is the scattering angle (the angle between the scattered ray and the direction of specular reflection);

α is the grazing angle;

λ is the wavelength of the X-ray;

$\psi(\theta)$ is the Point Response Function (PRF).

Let

$$2W_1(f, \lambda) = 2C_s e^{-f/f_s} f^{-1-\Delta s} + 2C_d q_s e^{-(f/f_d)^2} \frac{\lambda^2}{\sin^2 \alpha} f^{-1+\Delta d} \quad (3)$$

where

the first term on the right is due to the surface roughness scattering; the second term is due to the dust scattering.

C_s and C_d are simply proportional coefficients;

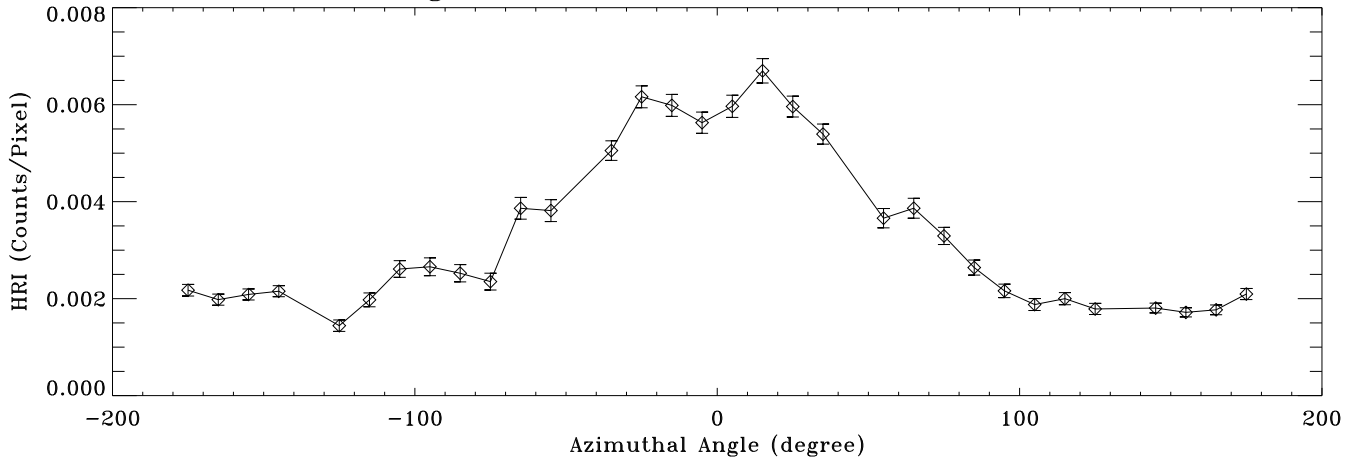
an exponential function in each term is used to add some curvature in case the scattering diminishes faster than a simple power law at larger angles, f_s and f_d are critical frequencies of the curvatures for surface roughness and dust scattering, respectively;

Δs and Δd are fitting parameters for the power law terms;

$q_s = (50\text{\AA}/\lambda)^{0.13}$ is an empirical function for the size-averaged dust grain scattering efficiency.

Before fitting equation (3) to the wing scan data, an aperture correction has to be made to the data. Since we used circular apertures of diameters ranging from 3 mm to 20 mm for the wing scan measurements, the data represent the average intensity, $I(r, a)$, within the aperture area, i.e. $I(r, a) = N(r, a)/\pi a^2 T$, where $N(r, a)$ is the total number of photons arrived in an aperture of radius a with offset r , within an integration time T . We need to know the surface brightness as a function of r , i.e. we need to know the intensity at the center of the aperture for each offset. Suppose that the surface brightness, $\psi(r)$, varies as a power law within each aperture area, i.e. $\psi(r) = Ar^{-\gamma}$,

Source: C-K, Ring Radius $r = 12.77$ mm
 Scattering in Annulus between $r-2.75$ mm and $r-0.17$ mm



Scattering in Annulus between $r+0.17$ mm and $r+2.75$ mm

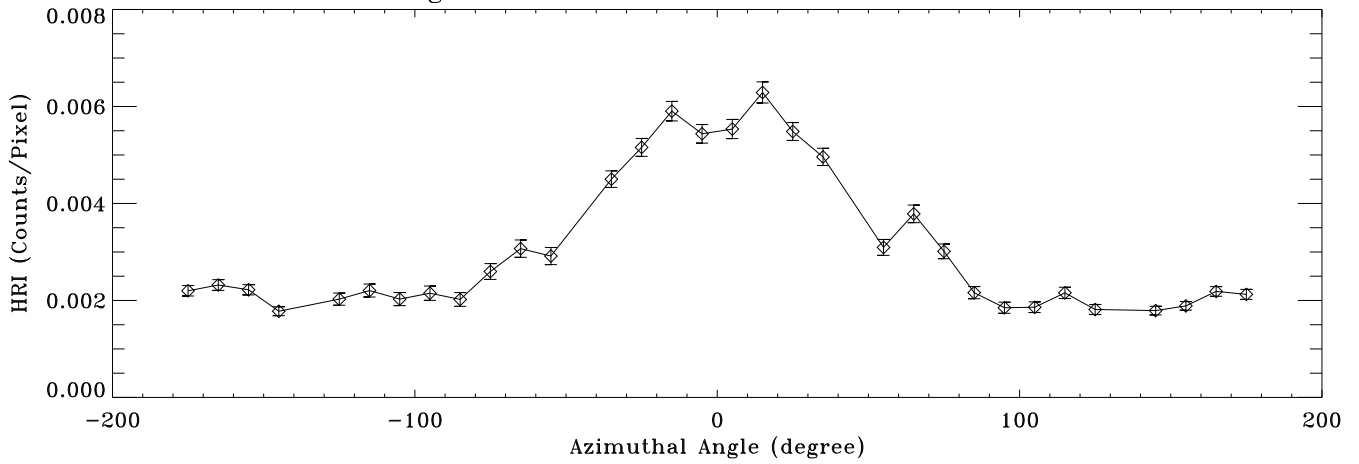


Figure 3: VETA-I ring focus dust scattering. Scattered photons around the ring as a function of the azimuthal angle, based on 4 HRI images taken 215.3 mm from the focal plane with a C-K source.

Source: Al-K, Ring Radius $r = 9.44$ mm
 Scattering in Annulus between $r-2.75$ mm and $r-0.15$ mm

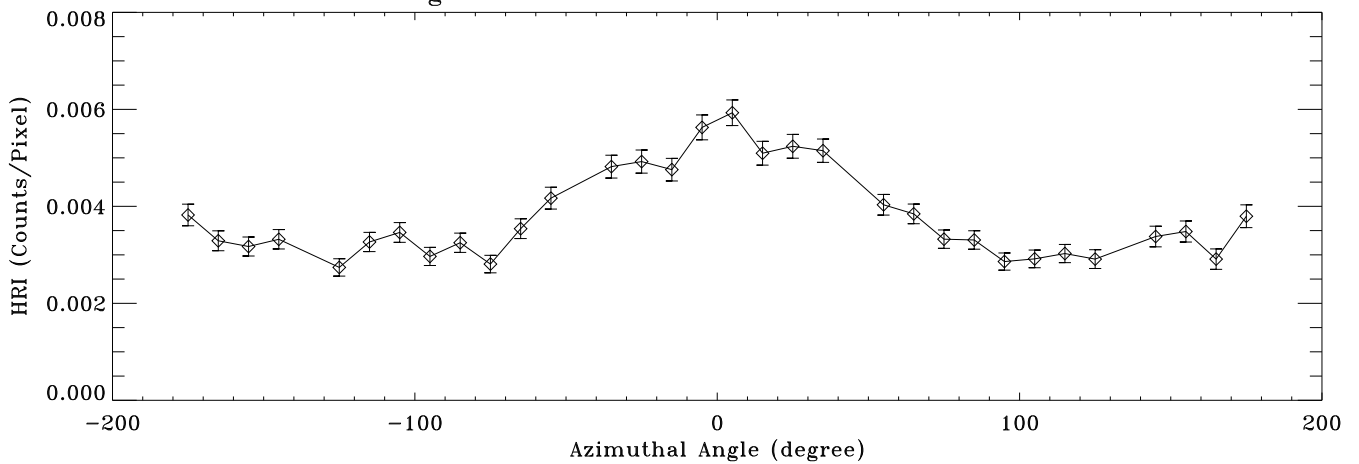


Figure 4: VETA-I ring focus dust scattering. Scattered photons around the ring as a function of the azimuthal angle, based on a HRI image taken 159.2 mm from the focal plane with an Al-K source.

where A is a proportional constant and γ is the power law index. It can be shown that

$$\psi(r) = \frac{I(r, a)}{{}_2F_1\left(\frac{\gamma}{2}, \frac{\gamma}{2}; 2; \frac{a^2}{r^2}\right)} \quad (4)$$

where ${}_2F_1$ is the normal hypergeometric function. All the VETA-I wing scan data were corrected by this aperture correction factor for the surface roughness and dust scattering analysis.

We then use equations (1), (2) and (3) to fit simultaneously all the aperture corrected VETA-I wing scan data. Figure 5 illustrates the analysis. The top panel shows the fit with the effective area per solid angle as a function of the offset angle. The middle panel shows the fit with PSD as a function of f . The bottom panel shows the fit with the dust scattering term properly subtracted. All the fitting parameters are shown on the bottom of Figure 5.

The $2W_1(f, \lambda)$ as obtained above is actually the sum of two PSDs, one for P1 and one for H1, since the measured scattering pattern was the result of two reflections. Assuming the surface qualities (both roughness and dust) are the same for P1 and H1, the PSD of each surface is one half of the value of $2W_1(f, \lambda)$ obtained above. To compare with the HDOS metrology data, we are interested in the surface roughness PSD for each surface (excluding the dust scattering term), $2W_{1,per-surface}$, which is

$$2W_{1,per-surface}(f) = C_s e^{-f/f_s} f^{-1-\Delta s} \quad (5)$$

This $2W_{1,per-surface}(f)$ is plotted in Figures 1 and 2 in comparison with the HDOS PSD. It agrees very well with the plot of $1.5 \times$ the PSD derived from the HDOS metrology data in Figure 2. (Long-dashed lines are compared with solid lines for $f > 1 \text{ mm}^{-1}$. The wing scan measurements are only sensitive in the frequency band of $f = 1 - 162 \text{ mm}^{-1}$.)

Given a surface roughness PSD function $2W_1$, the surface roughness amplitude RMS, σ , in frequency band $f_1 - f_2$ can be calculated as:

$$\sigma_{f_1-f_2}^2 = \int_{f_1}^{f_2} 2W_1(f) df \quad (6)$$

The VETA-I wing scan data covers the spatial frequency from 1 mm^{-1} to 162 mm^{-1} . Substituting equation (5) into the integral of (6), the RMS surface roughness in this band can be calculated. The RMS surface roughness beyond 162 mm^{-1} can be extrapolated. The results are (surface roughness amplitude RMS per surface, with 95% confidence error):

$$\sigma_{f=1-162} = 6.047 \pm 0.679 \text{ \AA}$$

$$\sigma_{f=162-1000} = 1.347 \pm 0.234 \text{ \AA} \quad (\text{Extrapolated})$$

$$\sigma_{f=1-1000} = 6.199 \pm 0.713 \text{ \AA} \quad (\text{Including extrapolated beyond } 162 \text{ mm}^{-1})$$

Compared with the surface roughness RMS computed earlier from the HDOS PSD (see Section 2 and Figures 1-2), the results here fit in between the HDOS PSD and $1.5 \times$ the HDOS PSD, and agree especially well with the $1.5 \times$ the HDOS PSD.

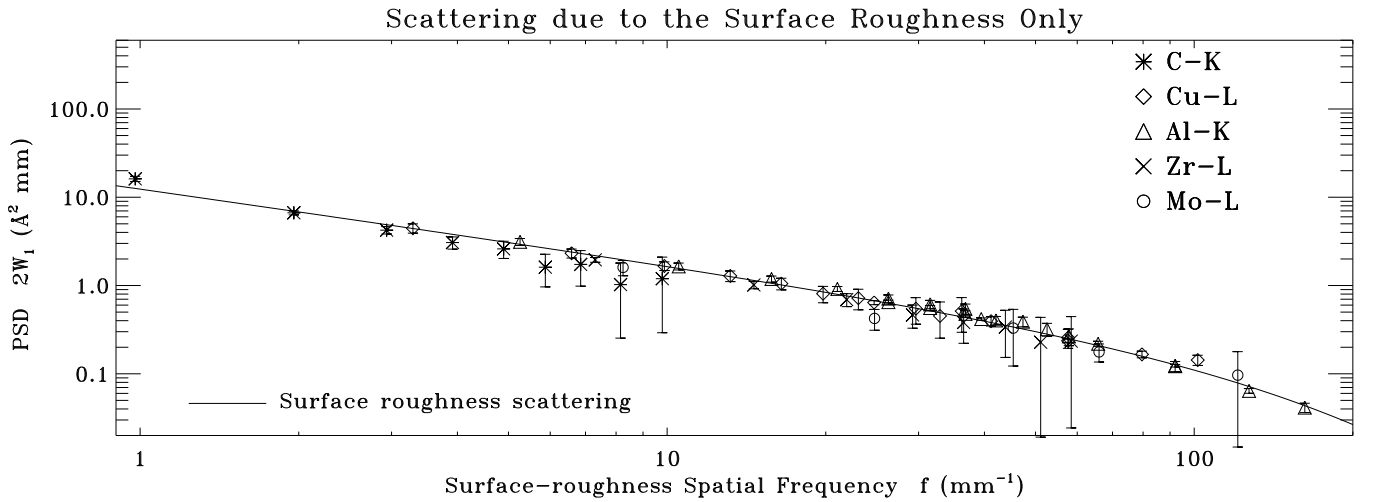
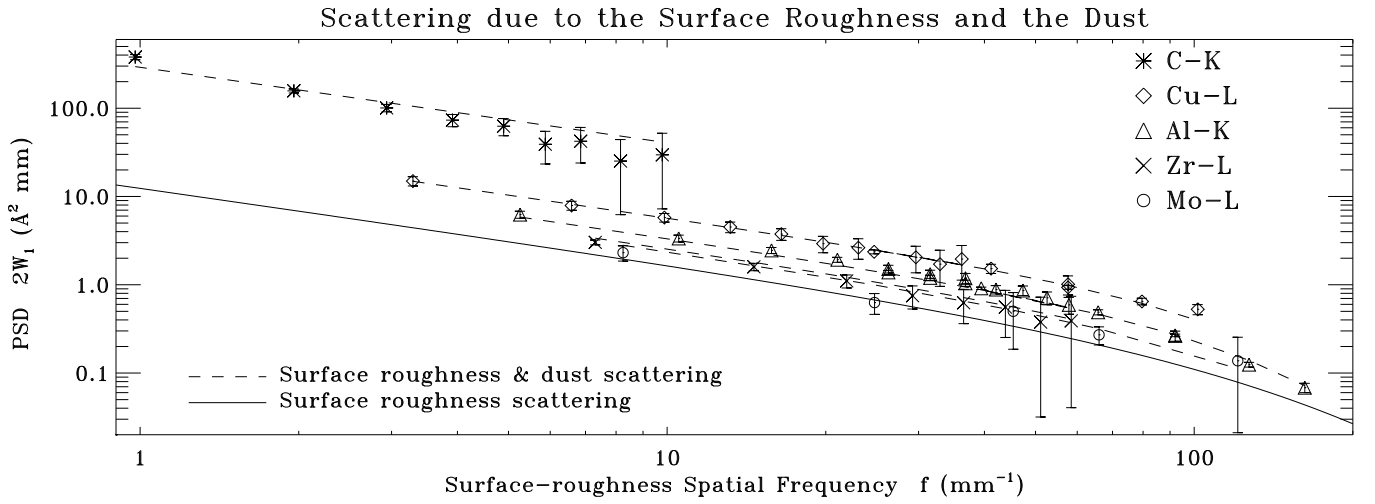
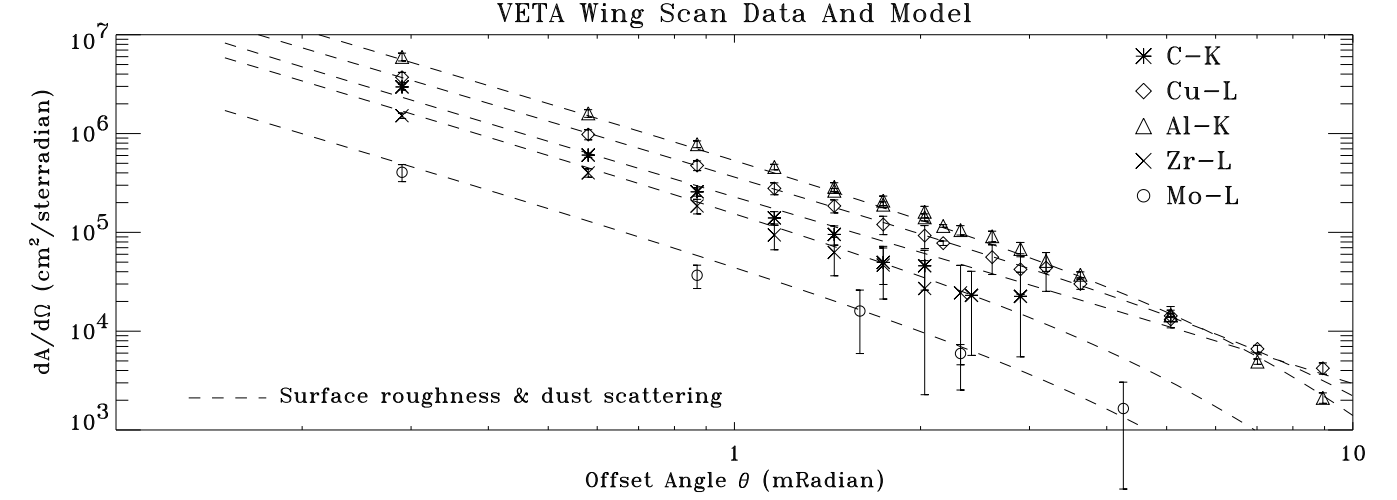
Based on our wing scan data analysis, the fractional VETA-I mirror surface covered by dust of grain radii a between $0.055 \text{ }\mu\text{m}$ and $10 \text{ }\mu\text{m}$ was calculated (with 95% confidence error):

$$F = (1.205 \pm 0.210) \times 10^{-4}$$

Using the best fitting parameters for equation (3), a dust scattering table was made for each energy. These dust scattering tables were then used in the VETA-I model for the simulation.

3.8 HRI detector resolution

The VETA-I ring focus measurement was made with an HRI X-ray detector, which is a microchannel plate with a resolution of $25 \text{ }\mu\text{m}$ (FWHM). The data were read out in 4096×4096 bins; each bin was $6.45 \text{ }\mu\text{m}$ by $6.45 \text{ }\mu\text{m}$. The model simulates the HRI detector: each incoming photon was blurred with a $25 \text{ }\mu\text{m}$ FWHM Gaussian function and then binned into one of the $6.45 \text{ }\mu\text{m}$ square bins.



$$2W_i(f, \lambda) = 2 C_s \exp(-f/f_s) f^{-1-\Delta s} + 2 C_p q_s \exp(-f^2/f_p^2) f^{1+\Delta p} \lambda^2 / \sin^2(\alpha)$$

$$q_s = (50 \text{ \AA} / \lambda)^{0.13} \quad f_s = 120 \text{ mm}^{-1} \quad f_p = 123.625 \text{ mm}^{-1}$$

$$C_s = 6.22924 \pm 0.764051 \text{ \AA}^2 \text{ mm} \quad \Delta s = -0.154134 \pm 0.0408675$$

$$C_p = 1.56143\text{e-}05 \pm 7.66543\text{e-}07 \text{ mm} \quad \Delta p = 0.149168 \pm 0.0226242$$

$$\text{Reduced } \chi^2 = 1.220 \quad \text{Probability} = 0.127$$

$$\text{Surface Roughness per Surface } \sigma_{f=1-162} = 6.047 \pm 0.679 \text{ \AA}$$

Figure 5: VETA-I mirror surface roughness and dust scattering analysis using the wing scan data.

4 RESULTS

Having established the VETA-I model, massive computer time was devoted to the actual simulation – the ray-tracing. The ray-tracing tool was developed by the SAO AXAF Mission Support team, based on an older NASA program – OSAC [10].

4.1 Full Width Half Maximum

The FWHM of the VETA-I focus was measured in the focal plane with pinhole scans in both Y (horizontal) and Z (vertical) directions. The pinhole size was $5\ \mu\text{m}$, the step size was $2\ \mu\text{m}$, and the scan steps were 80. The X-ray source used was Al-K. The ray-tracing simulates exactly the same situation: first, a large number of rays were traced through the VETA-I model (3 million in the case of FWHM), and their positions in the focal plane were recorded. Then the numbers were counted for rays falling into a $5\ \mu\text{m}$ diameter circle moving along Y or Z direction. Figure 6 compares the results of the ray-tracing and the X-ray test data. Although there are some discrepancies at the bottom, the agreement on the FWHM is reasonably good. Table 2 lists the measured and simulated FWHM in both Y and Z directions.

Table 2. VETA-I Full Width Half Maximum

Direction	Measured	Simulated
Y-Scan	0.219 ± 0.017 arcsec	0.234 arcsec
Z-Scan	0.217 ± 0.017 arcsec	0.221 arcsec

4.2 Effective area

The total effective area (or simply Effective Area) is the total power reflected by the VETA-I into 2π steradians centered at the focus, measured in units of cm^2 . It is equal to the projected area of an equivalent mirror with 100% reflectivity, or a projected area of $P1 \times R^2(E, \alpha)$, where R is the mirror reflectivity as a function of X-ray energy E and grazing angle α . The effective area within 10 mm radius of the focus was measured with a 20 mm diameter aperture for each of the five energies. The effective area outside the 10 mm radius was extrapolated using a curved power law, $\psi(r) = Ar^{-\gamma}e^{-r/r_c}$, fitted to the aperture corrected wing scan data (see Section 3.7). For the wing scan measurements of Zr-L and Mo-L, there were not enough far-off-axis data to give the correct curvature to the power law. We have fixed the curvatures of the wing scan data for these two sources using the curving distance r_c obtained from the wing scan data of Al-K, i.e. let $r_{c,S} = r_{c,Al-K} \lambda_S / \lambda_{Al-K}$, where $S = \text{Zr-L}$ or Mo-L .

Table 3 lists the VETA-I effective area. Columns 1 and 2 list the sources and corresponding energies; column 3 is the measured effective area for $r < 10$ mm; column 4 is the extrapolated effective area for $r > 10$ mm; column 5 is the total effective area, i.e. the sum of column 3 and 4; column 6 is the total effective area simulated by the VETA-I model.

Table 3. VETA-I Effective Area (Units: cm^2)

Source	Energy (keV)	Effective Area $r < 10\text{mm}$	Effective Area $r > 10\text{mm}$	Total Effective Area 2π steradians	Simulated Total Effective Area
C-K	0.277	222.83	4.37	227.20 ± 2.43	228.17
Cu-L	0.932	187.63	6.92	194.55 ± 2.72	193.85
Al-K	1.488	178.22	6.92	185.14 ± 1.38	184.92
Zr-L	2.067	34.99	1.23	36.22 ± 3.80	38.94
Mo-L	2.334	8.50	0.32	8.82 ± 1.07	8.11

An apodizer correction has to be made to the simulated effective area curve. The apodizers were located at the back ends of P1 and H1 and measured radially inward from the optical surface as 0.048 ± 0.009 inches (1.22 ± 0.23 mm) for P1, and 0.043 ± 0.009 inches (1.09 ± 0.23 mm) for H1. The uncertainty of 0.23 mm on both apodizers could have

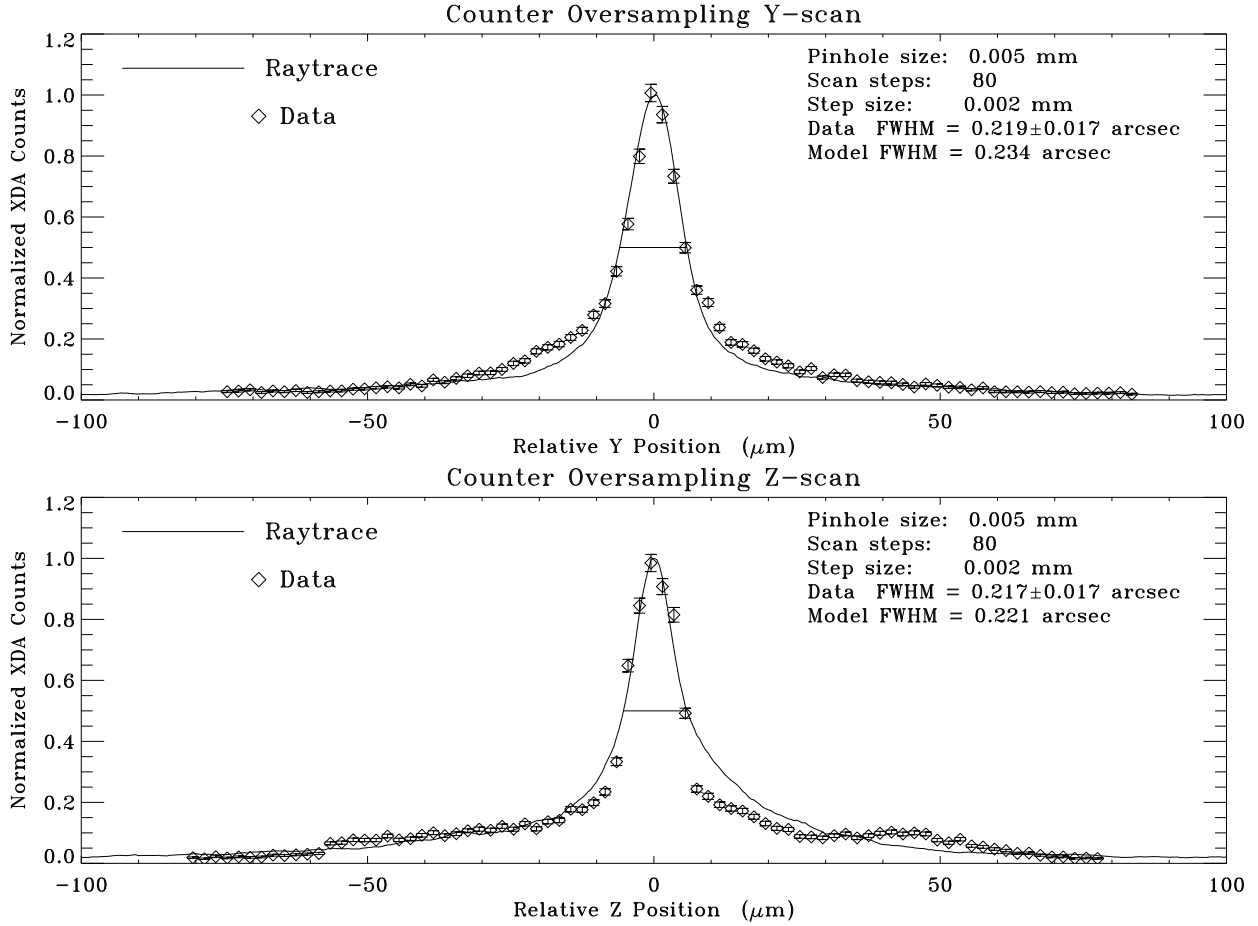


Figure 6: VETA-I FWHM data compared with the VETA-I model.

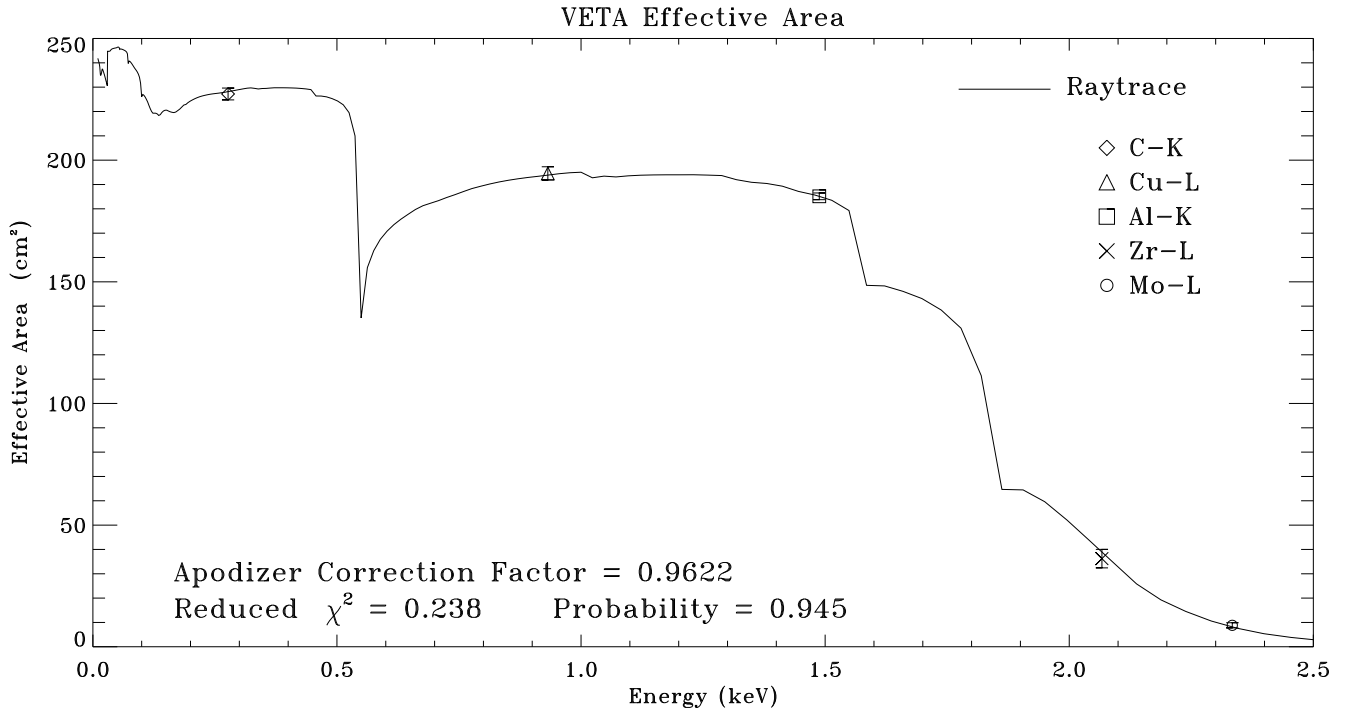


Figure 7: VETA-I effective area data compared with the VETA-I model.

introduced an uncertain factor between 0.938 to 1.067 for the absolute value of the effective area for all of the energies. To obtain a good fit, the simulated effective area curve has to be corrected by a factor of 0.962 which is within the uncertain range due to the apodizers' position. Thus, by comparing the simulation and the measurements, we can actually estimate the apodizer positions. In this case, we conclude that the apodizers are positioned radially inward more than the specified values, but are within the quoted errors. However, this is the combined effect of both apodizers. We can not give the exact location for each apodizer.

From now on, this apodizer correction factor of 0.962 is applied to all the following simulations whenever the absolute value is concerned.

A total of 15.6 million rays were traced to simulate the VETA-I effective area (241 energy steps from 0.01 keV to 2.5 keV with 64675 rays at each energy). Figure 7 shows the simulated effective area curve after the apodizer correction with the measured effective area at five energies. The fit is excellent.

4.3 Encircled energy

The encircled energy was measured with a series of apertures with diameters ranging from $5\mu\text{m}$ to 20 mm. (There were 16 apertures with diameters of 0.005, 0.01, 0.025, 0.05, 0.1, 0.3, 0.5, 0.75, 1, 1.5, 2, 3, 5, 7.5, 10, 20 mm.) There was a complication called "the wire mesh effect" [11]: The proportional counter used for the measurement has a thin plastic window with an opaque wire mesh supporting grid. Depending on the counter position, this mesh can cause the X-ray transmission to vary as much as $\pm 9\%$, which directly translates into an error in the encircled energy. In order to correct this wire mesh effect, window scan measurements were made for sources of C-K, Al-K and Zr-L, in which the counter was scanned in both horizontal (Y) and vertical (Z) directions with the aperture fixed. The mesh effects were corrected for these three energies after analyzing the window scan data. However, there was no window scan measurement made for Cu-L and Mo-L. The mesh effects for these two energies were estimated based on window scan measurements on other energies. Therefore the encircled energy data of C-K, Al-K and Zr-L have smaller uncertainties because the window scan measurements were made.

Five panels in Figure 8 show the simulated encircled energy curve with the encircled energy data, for all 5 measured X-ray energies. The solid lines are the ray-trace results, after applying the apodizer correction factor of 0.962 and a normalization factor in order to obtain the best fit to the large apertures (0.3 mm to 20 mm). This normalization factor is different for each energy. Therefore it is not due to the apodizer. Several possible factors could have caused this: 1) measurement errors; 2) the actual source spectrum has one or two main lines, several satellite lines and a continuum, the simulation used a monochromatic centroid energy to represent each source; 3) uncertainty in the optical constants. An example for the last possible cause is Zr-L, which needs a larger correction and its energy is near the edge where the optical constant changes rapidly with energy.

At this point we would like to test the sensitivity of the HDOS metrology measurements. We multiplied the HDOS PSD data and the HDOS map data by factors ranging from 0.5 to 2.0 and repeated the simulations. For the PSD data (mainly the WYKO measurements), we found that a factor of 1.5 increase gives a better fit (smaller reduced χ^2); when this factor increases to 2.0, the fit becomes worse. For the map data, the best fit is when the factor is in between 1 (i.e. no change) and 1.5. Dotted lines in Figure 8 are the results of $1.5 \times$ HDOS PSD and map. Dashed lines are the results of $2 \times$ HDOS PSD and map. (For clarity reasons, we did not plot all the cases we studied). Table 4 lists the parameters for the VETA-I encircled energy fits. The third column in Table 4 is the input of the HDOS data in the VETA-I model. The fourth column is the effective area correction factor, which is the division of column 5 by column 6 in Table 3. This is the offset of the total effective area of each energy (measured with the 20 mm aperture and extrapolated to 2π steradians with the wing scan data) from the simulated total effective area curve. The fifth column is the normalization factor mentioned above. The differences between columns 4 and 5 are mainly due to the extrapolations made for the total effective area. The sixth column is the Reduced χ^2 for fitting all the apertures. The seventh column is the reduced χ^2 for fitting the large (0.3 mm – 20 mm) apertures, where window scan measurements were made for C-K, Al-K and Zr-L.

6.5 million rays were traced for each case presented in Figure 8. Thus the 15 curves in Figure 8 represent the results of tracing nearly 100 million rays.

In general, the simulations agree with the data reasonably well. The normalization factors are 0.98 or above (except for Zr-L) for $1.5 \times$ HDOS PSD. Zr-L has a normalization factor of 0.93 which agrees with its effective area

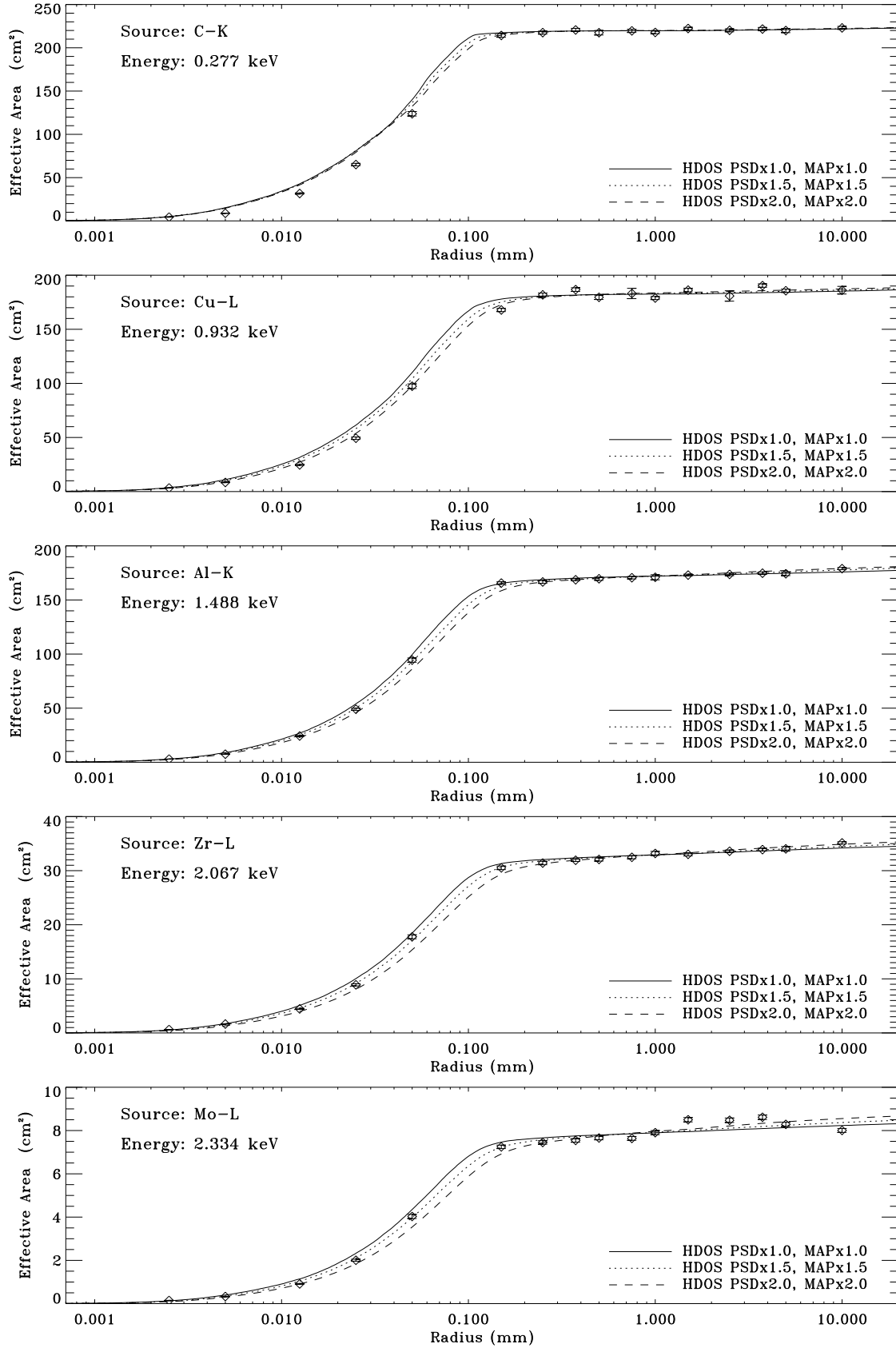


Figure 8: VETA-I encircled energies data compared with the VETA-I model.

Table 4. VETA-I Encircled Energy Fit to the VETA-I model

Source	Energy (keV)	HDOS Data	Effective Area Corr. Factor	Norm. Factor	Reduced χ^2 All Aps.	Reduced χ^2 Large Aps.
C-K	0.277	PSD \times 1.0, map \times 1.0	0.996 \pm 0.011	0.996	111.8	0.973
		PSD \times 1.5, map \times 1.0	0.996 \pm 0.011	0.998	109.5	0.798
		PSD \times 1.5, map \times 1.5	0.996 \pm 0.011	0.998	105.6	0.809
		PSD \times 2.0, map \times 2.0	0.996 \pm 0.011	1.000	89.4	0.693
Cu-L	0.932	PSD \times 1.0, map \times 1.0	1.004 \pm 0.014	0.976	37.1	8.538
		PSD \times 1.5, map \times 1.0	1.004 \pm 0.014	0.981	17.0	6.345
		PSD \times 1.5, map \times 1.5	1.004 \pm 0.014	0.981	19.2	6.129
		PSD \times 2.0, map \times 2.0	1.004 \pm 0.014	0.989	7.6	4.658
Al-K	1.488	PSD \times 1.0, map \times 1.0	1.001 \pm 0.008	0.958	10.8	1.747
		PSD \times 1.5, map \times 1.0	1.001 \pm 0.008	0.985	4.8	1.092
		PSD \times 1.5, map \times 1.5	1.001 \pm 0.008	0.985	4.7	1.262
		PSD \times 2.0, map \times 2.0	1.001 \pm 0.008	0.989	9.6	4.532
Zr-L	2.067	PSD \times 1.0, map \times 1.0	0.930 \pm 0.098	0.912	9.2	3.888
		PSD \times 1.5, map \times 1.0	0.930 \pm 0.098	0.932	5.2	1.464
		PSD \times 1.5, map \times 1.5	0.930 \pm 0.098	0.931	4.9	1.607
		PSD \times 2.0, map \times 2.0	0.930 \pm 0.098	0.959	19.4	2.041
Mo-L	2.334	PSD \times 1.0, map \times 1.0	1.087 \pm 0.132	0.943	25.4	11.28
		PSD \times 1.5, map \times 1.0	1.087 \pm 0.132	0.982	12.2	8.261
		PSD \times 1.5, map \times 1.5	1.087 \pm 0.132	0.978	13.4	8.653
		PSD \times 2.0, map \times 2.0	1.087 \pm 0.132	1.017	18.5	9.894

correction factor, which is probably due to the optical constant used, as previously mentioned. All the normalization factors agree with the effective area correction factors within 2% (except for Mo-L). This means that the encircled energy fits are consistent with the effective area fit, i.e. the extrapolations made for the total effective area are accurate to 2%. The Mo-L data were not very good. It is seen in the bottom panel of Figure 8 that the 3 mm, 5 mm and 7.5 mm apertures had significantly higher counts than the rest of the large apertures (ranging from 0.3 mm to 20 mm). The cause of this anomaly is unknown. The window scan measurements were not done for the Mo-L source. Also, the source had larger variations during the Mo-L data taking. For low energies (C-K and Cu-L), data of small apertures fall below the simulated curve. For Al-K and Zr-L, the data agree very well with simulations based on 1.5 \times HDOS PSD.

We thus suggest that the actual surface roughness of VETA-I could be larger (but within 50%) than the PSD according to the HDOS WYKO data. This could be due to: 1) the WYKO measurement uncertainly; 2) the sampled area of the WYKO measurement was underrepresented; 3) the WYKO data exist only for P1 and we used them for both P1 and H1.

4.4 Wing scan

The VETA-I wing scan measurements were made with 3 mm, 7.5 mm and 20 mm apertures scanned in both Y and Z directions. The step size was 3 mm. Each scan went as far from the focus as possible until the signal was comparable to the statistical noise. It went 92.5 mm off axis with the 20 mm aperture for sources Cu-L and Al-K.

Figure 9 shows the simulated wing scan curve with the wing scan data. (Since the simulations were made as photons falling into the area of actual circular apertures, there were no aperture corrections involved here for either the data or the model.) To test the sensitivity of the HDOS metrology measurements, we again multiplied the HDOS PSD data and the HDOS map data by factors ranging from 0.5 to 2.0 and repeated the simulations. We again found that multiplying by a factor of 1.5 to the HDOS PSD data gives a better fit; while the best fit for the map data is when the factor is between 1 and 1.5. Figure 9 also represents the results of ray-tracing nearly 100 million rays, the

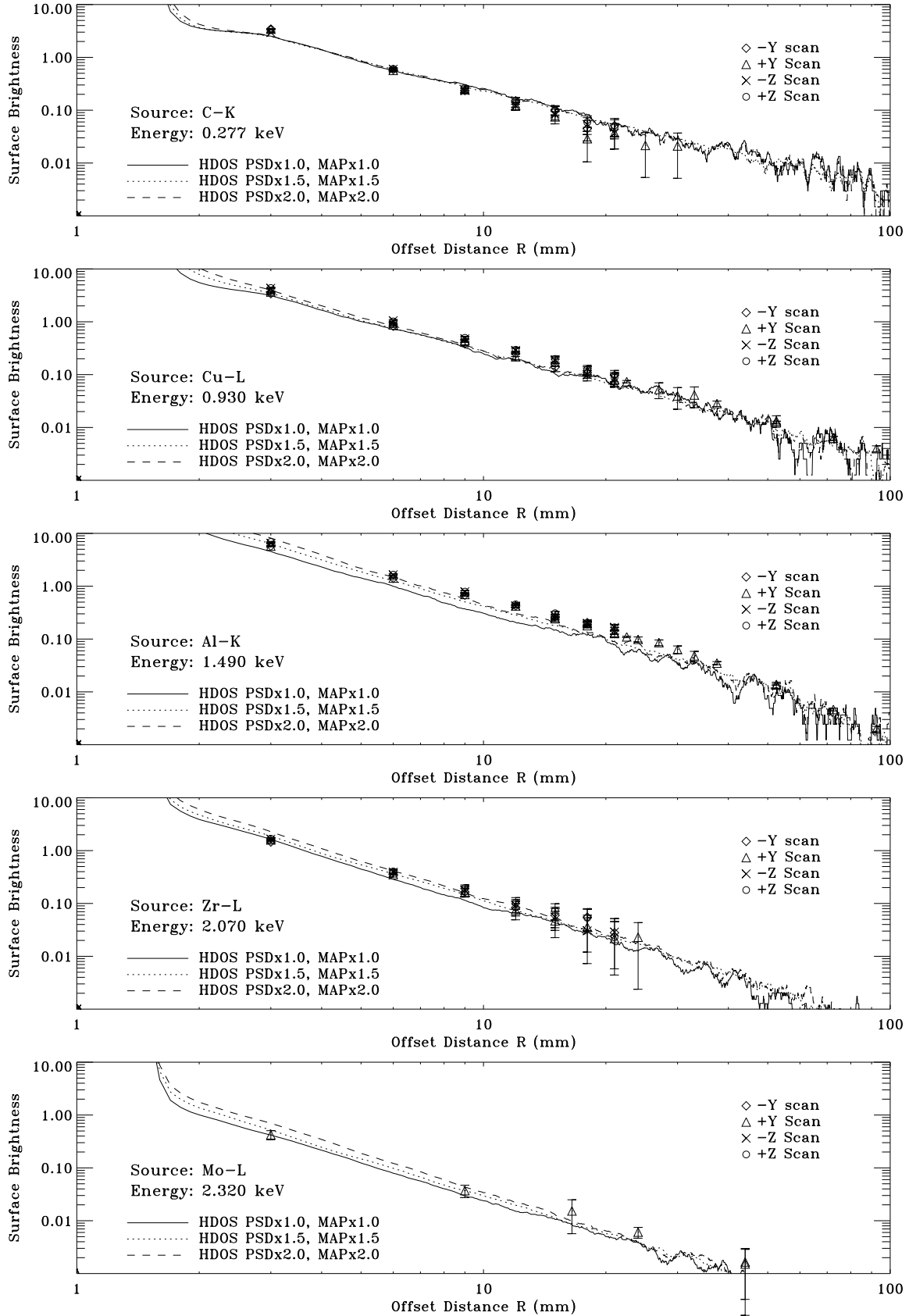


Figure 9: VETA-I wing scan data compared with the VETA-I model. (Surface brightness is in units of effective area per unit aperture area: cm^2/cm^2 .)

same as Figure 8.

The simulations agree with the data within the measurement errors, except for AL-K, where data is above the simulated curve.

4.5 Ring focus

The VETA-I mirror ring focus measurements were made with an HRI (microchannel plate) X-ray detector. The HRI was placed 215.3 mm from the focal plane and images were taken. Because the ring diameter (25.5 mm) was larger than the HRI, four images were taken for top, bottom, left and right quadrants of the ring. Each image had an exposure time of 30 minutes. The C-K source was used for the measurements. In Figure 10, the top panel shows a plot of the ring width RMS versus the azimuthal angle. (We chose RMS to represent the ring width because it carries a better statistical value than FWHM.) When looking towards the HRI detector, 0° is on the bottom of the ring; 90° is on the left; 180° is on the top; and -90° is on the right. A modulation with a 30° period is clearly shown in this figure. The bottom panel of Figure 10 shows the Fourier transformation of the top panel, plotted as the modulation amplitude RMS versus the frequency in one circumference. The modulation has dominant frequencies of 2 (180° period), 12 (30° period) and its higher harmonics. With the HRI images, we can also obtain the ring mean radius as a function of the azimuthal angle. The appeared ring radius variation is a summed effect of mirror metrology errors, mirror roundness errors $\Delta\Delta R$, mirror axial slope errors, mount induced errors, and the HRI detector errors. It has been shown that the HRI detector nonuniformity is the dominant factor here [12].

We again multiplied the HDOS PSD and map data by factors ranging from 0.5 to 2.0 to simulate the ring focus measurements. 20 million rays were traced for each case. We again found that a factor of 1.5 gives a better fit; Figure 11 shows the same analysis for the simulated ring focus results with $1.5 \times$ HDOS PSD and map. The base line and the modulation amplitude of the simulated ring width RMS are similar to those measured. The simulation has stronger 2-fold symmetry, weaker 12 fold symmetry and stronger higher harmonics of the 12 fold. The multi-symmetries of the ring width RMS would not be affected by the scattering. They are mainly due to the mount induced distortions. This means that improvements can be made by SAO on these models.

We now define a quantity called ‘‘Azimuthal Distribution of RMS Image Core’’, S , as follows:

$$S = [(r - \bar{r})^2 + \sigma_r^2 - \sigma_{HRI}^2 - \sigma_{source}^2]^{1/2} \quad (7)$$

where r is the radius of the ring; \bar{r} is the mean radius; σ_r is the RMS of the ring width; σ_{HRI} is the RMS of the HRI resolution; σ_{source} is the RMS of the source extension. Quantity S , as a function of the azimuthal angle, represents the ring width and radius variations after the system effects are removed. Thus it is a measure of the mirror surface quality.

Figure 12 compares the probability distribution of S between the ring focus data and the simulated case shown in Figures 10 and 11. It is seen that, for the simulation with $1.5 \times$ HDOS PSD and map, the distribution of S is very similar to the data and the mean S , \bar{S} , agrees very well with the data. This means, once again, that the $1.5 \times$ HDOS PSD and map gives a reasonable description of the VETA-I mirror surface.

The ring focus measurements give a ring radius RMS of 0.255 arcsec which is dominated by the HRI errors. This means that the actual ring radius RMS should be smaller. Meanwhile, the simulation gives a ring radius RMS of 0.143 arcsec, which is due to the HDOS data and the mount induced distortions. Thus this study gives at least a sanity check for the HDOS metrology measurements with an accuracy less than 0.255 arcsec for the radius RMS in the ring focus image (and probably significantly less because of the HRI uncertainties).

5 CONCLUSIONS

From this study, we draw the following conclusions:

- The method used for the HDOS metrology measurements covers the frequency range of interest for AXAF-I.
- The VETA-I test results agree with the VETA-I model reasonably well.
- The VETA-I test results agree best when the PSD derived from the HDOS WYKO data is multiplied by a factor of 1.5. The best fit for the map data is when this ‘increasing’ factor is between 1 and 1.5. This ‘increasing’

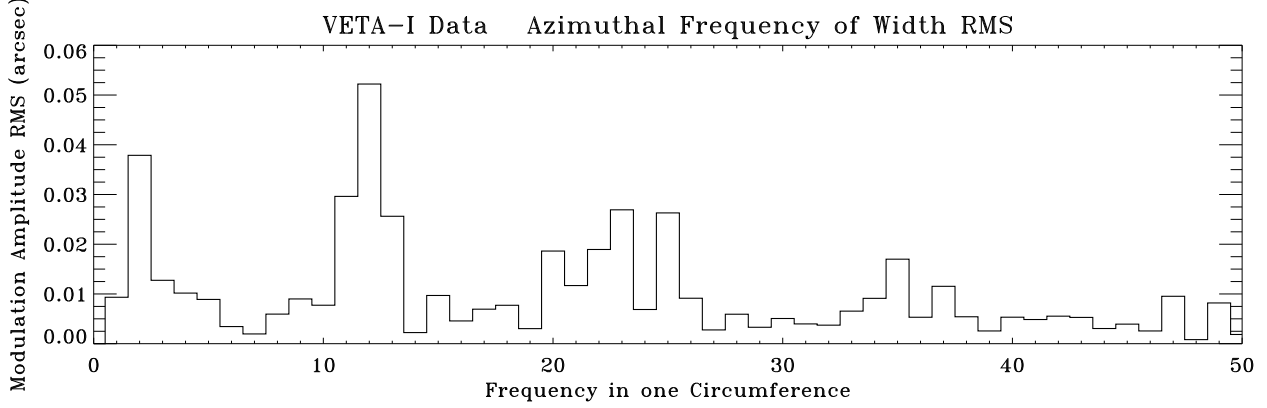
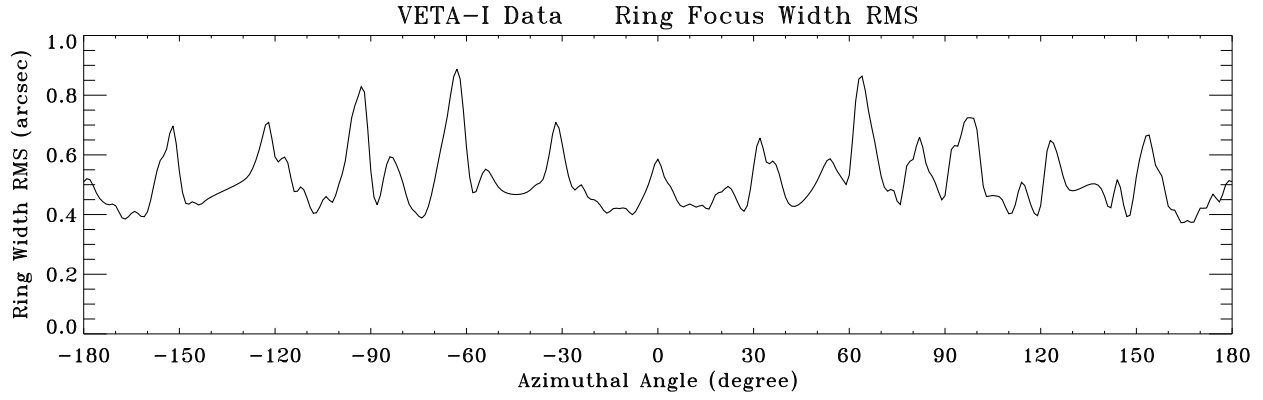


Figure 10: VETA-I ring focus data.

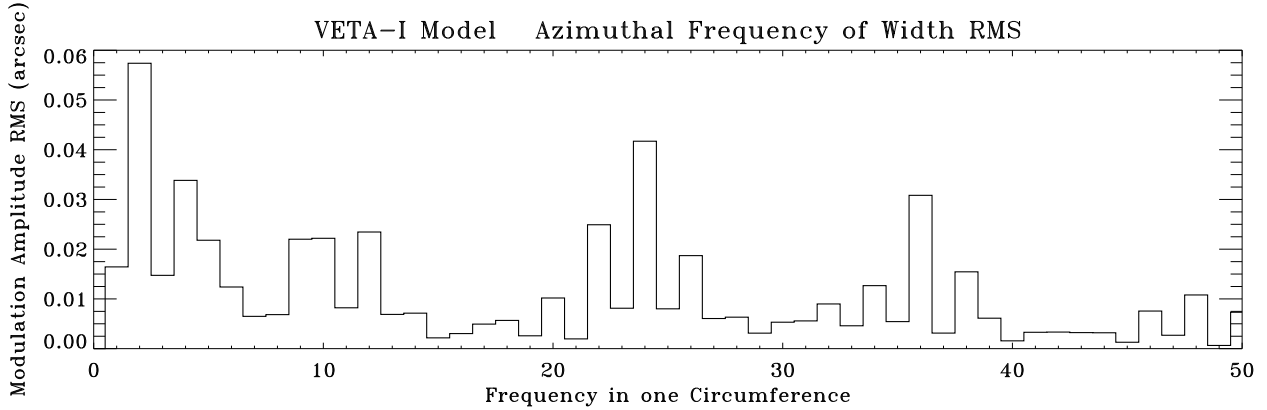
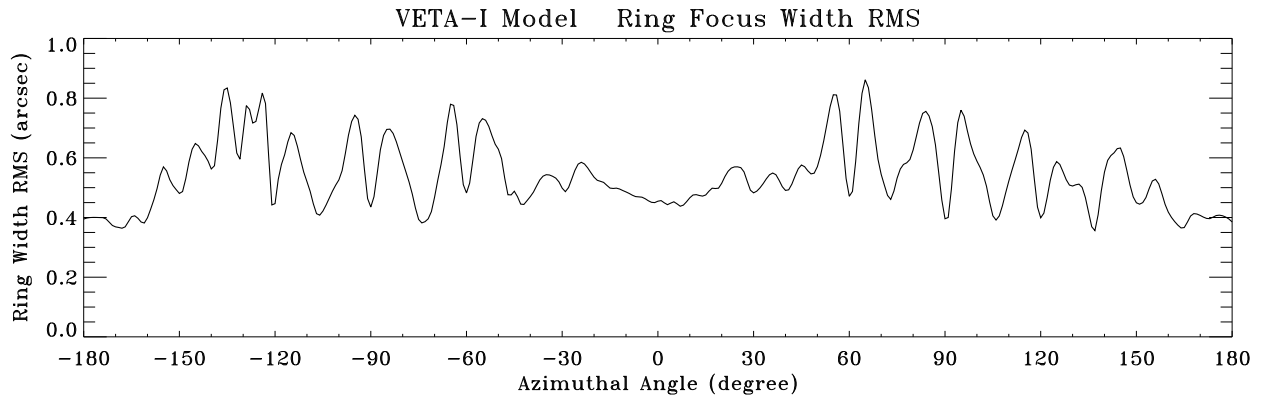


Figure 11: VETA-I ring focus model with $1.5 \times$ HDOS PSD and map.

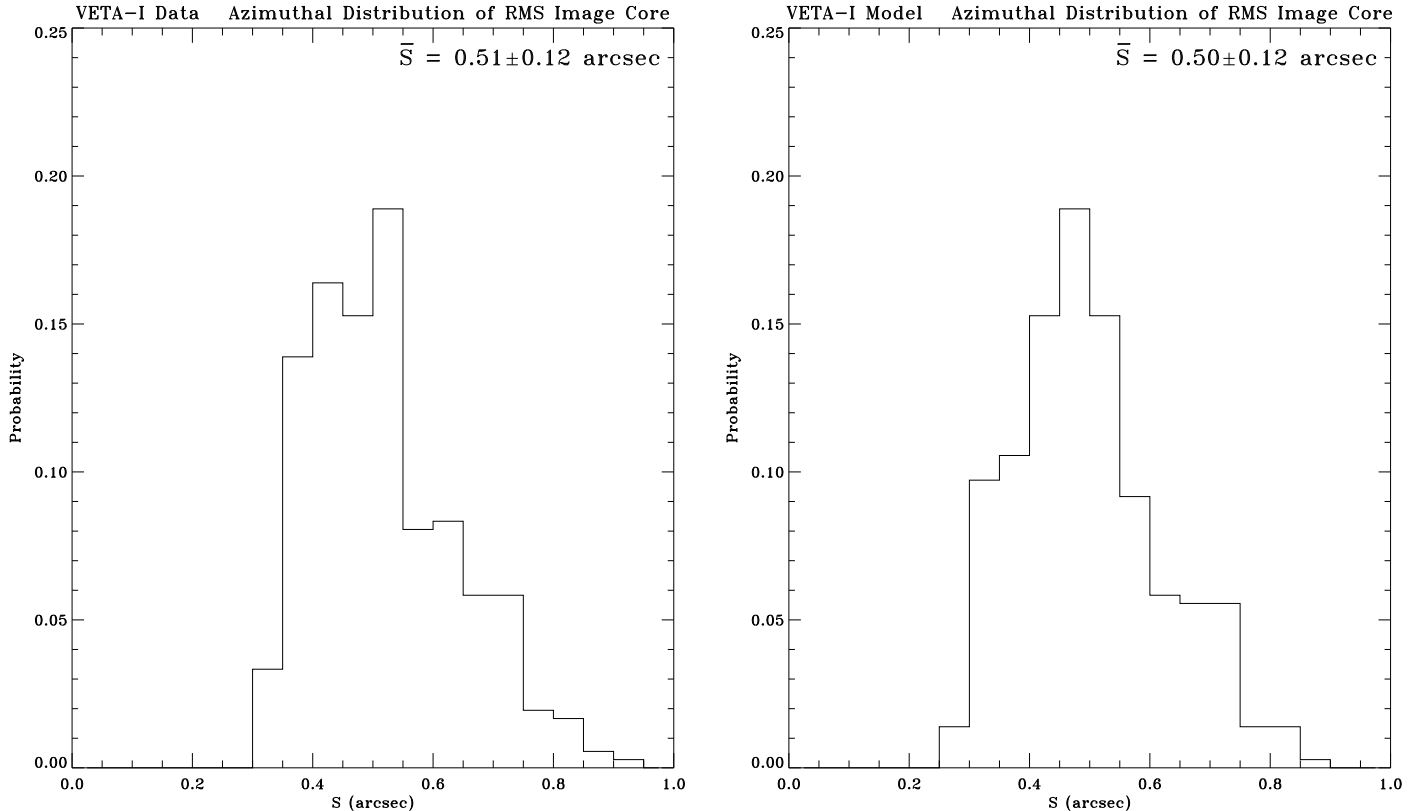


Figure 12: VETA-I ring focus azimuthal distribution of RMS image core. VETA-I model is with $1.5 \times$ HDOS PSD and map.

factor has been required consistently throughout the analyses of the VETA-I encircled energy, wing scan and ring focus data. This required factor could either represent a disagreement between the X-ray test data and the predicted results or, more likely, be a consequence of the assumption that the unmeasured H1 is similar to P1.

- The VETA-I test results serve at least as a sanity check for the HDOS CIDS metrology with an accuracy of <0.255 arcsec RMS radius of the focused image, indicating no major metrology errors. There is agreement between predicted and measured performance to within the uncertainties caused by incomplete metrology data and experimental errors.
- Similar analysis can be and should be performed on the HRMA X-ray test data, which is an important step in securing a scientifically successful AXAF mission.

6 ACKNOWLEDGMENTS

We would like to thank the SAO AXAF Mission Support team, especially Lester Cohen, Mark Freeman, Terry Gaetz, Diab Jerius and Bill Podgorski, for their efforts in building the VETA-I model and allowing us to use the ray-tracing software they have developed. The mirror surface dust scattering model used in this analysis was mainly based on studies by Steve O'Dell and Ron Elsner.

References

- [1] P. Zhao, E. M. Kellogg, D. A. Schwartz, Y. Shao, and M. A. Fulton, "Intensity Distribution of the X-ray Source for the AXAF VETA-I Mirror Test," *SPIE Proceedings* Vol. 1742, 26, San Diego, 1992.

- [2] P. Zhao, M. D. Freeman, D. Jerius, and Y. Shao, “AXAF VETA-I Mirror Ring Focus Measurements”, *SPIE Proceedings* Vol. 2011, 59, San Diego, 1993. (Figure 1 illustrates the X-ray test geometry.)
- [3] D. E. Zissa, “Comparison of Ring-focus Image Profile with Predictions for the AXAF VETA-I Test”, *SPIE Proceedings* Vol. 1742, 91, San Diego, 1992.
- [4] “Multilayer and Grazing Incidence X-ray/EUV Optics for Astronomy and Projection Lithography”, *SPIE Proceedings* Vol. 1742, pp. 1-202, San Diego, 1992; “Multilayer and Grazing Incidence X-ray/EUV Optics II”, *SPIE Proceedings* Vol. 2011, pp. 59-74, San Diego, 1993. Editors: R. B. Hoover and A. B. C. Walker, Jr.
- [5] P. Beckmann and A. Spizzichino, “The Scattering of Electromagnetic Waves from Rough Surfaces”, Pergamon Press, 1963.
- [6] B. L. Henke, E. M. Gullikson, and J. C. Davis, “X-ray Interactions: Photoabsorption, Scattering, Transmission, and Reflection at $E = 50\text{--}30000$ eV, $Z = 1\text{--}92$ ”, *Atomic Data and Nuclear Data Tables*, 54(2), 181, 1993.
- [7] S. L. O’Dell, R. F. Elsner, J. J. Kolodziejczak, M. C. Weisskopf, J. P. Hughes, and L. P. Van Speybroeck, “X-ray Evidence for Particulate Contamination on the AXAF VETA-I Mirrors”, *SPIE Proceedings* Vol. 1742, 171, 1992.
- [8] R. F. Elsner, “VETA Wing Scan Analysis”, memorandum to Leon P. Van Speybroeck, January 11, 1994.
- [9] Strictly speaking, the surface power spectral density (PSD), $2W_1$, is defined as the Fourier transform of the surface correlation function. Under the smooth-surface approximation, $2W_1$ is equal to the right-hand side of equation (2). We have used one-sided PSD here. So that the total power is the integral of $2W_1$ from $f = 0$ to $f = \infty$, i.e. $\sigma^2 = \int_0^\infty 2W_1(f)df$, where σ is the total surface roughness amplitude RMS.
- [10] D. Jerius, M. D. Freeman, T. Gaetz, J. P. Hughes, and W. Podgorski, “The SAO AXAF Simulation System”, ADASS Conference, Baltimore, 1994.
- [11] P. Zhao, M. D. Freeman, J. P. Hughes, E. M. Kellogg, and D. T. Nguyen, “AXAF VETA-I Mirror Encircled Energy Measurements and Data Reduction”, *SPIE Proceedings* Vol. 1742, 75, San Diego, 1992.
- [12] P. Zhao, “VETA-I Ring Focus Test Data”, report presented on EKC PMMR, December 16, 1993. SAO document: SAO-AXAF-DR-95-146.